Hindrance of heavy-ion fusion at extreme sub-barrier energies in open-shell colliding systems

C. L. Jiang, K. E. Rehm, H. Esbensen, R. V. F. Janssens, B. B. Back, C. N. Davids, J. P. Greene, D. J. Henderson, C. J. Lister, R. C. Pardo, T. Pennington,* D. Peterson, D. Seweryniak, B. Shumard, S. Sinha, X. D. Tang, I. Tanihata, and S. Zhu
Physics Division, Argonne National Laboratory, Argonne, Illinois 60439, USA

P. Collon and S. Kurtz
University of Notre Dame, Notre Dame, Indiana 46556, USA

M. Paul
Hebrew University, Jerusalem 91904, Israel
(Received 20 December 2004; published 29 April 2005)

The excitation function for the fusion-evaporation reaction ^{64}Ni + ^{100}Mo has been measured down to a cross section of ∼5 nb. Extensive coupled-channels calculations have been performed, which cannot reproduce the steep falloff of the excitation function at extreme sub-barrier energies. Thus, this system exhibits a hindrance for fusion, a phenomenon that has been discovered only recently. In the *S*-factor representation introduced to quantify the hindrance, a maximum is observed at $E_s = 120.6$ MeV, which corresponds to 90% of the reference energy E_s^{ref}, a value expected from systematics of closed-shell systems. A systematic analysis of Ni-induced fusion reactions leading to compound nuclei with mass $A = 100$–200 is presented in order to explore a possible dependence of fusion hindrance on nuclear structure.

DOI: 10.1103/PhysRevC.71.044613 PACS number(s): 25.70.Jj, 24.10.Eq

I. INTRODUCTION

Heavy-ion-induced fusion reactions have been studied extensively for more than forty years, especially since the discovery of the sub-barrier enhancement phenomenon [1–5]. Coupled-channels descriptions appear to explain the phenomenon successfully [6,7]. Recently, however, evidence was found of a strong hindrance of the fusion process at extreme sub-barrier energies, an effect for which there is no satisfactory explanation in present model calculations [8]. A sensitive method for identifying this sub-barrier hindrance is provided by expressing the cross section σ in terms of the S factor

$$S = \sigma E \exp(2\pi\eta), \tag{1}$$

where $\eta = Z_1 Z_2 e^2/(\hbar v)$ is the Sommerfeld parameter and E is the center-of-mass energy [9]. A systematic survey of existing data from the literature shows that there is a regular pattern to the energy dependence for the appearance of fusion hindrance [9]. For stiff, closed-shell colliding systems, a significant maximum in the S factor is present as a function of the beam energy. This maximum signals the onset of sub-barrier hindrance, and the energy E_s at which it is located can be described well by an empirical formula [9]

$$E_s^{\mathrm{ref}} = 0.356(Z_1 Z_2 \sqrt{\mu})^{\frac{2}{3}}\ (\mathrm{MeV}), \tag{2}$$

where $\mu = A_1 A_2/(A_1 + A_2)$. For softer systems, this formula provides an upper limit for the energy at which the S factor has its maximum.

Fusion hindrance at extreme sub-barrier energies is relevant to understanding not only the dynamics of reactions between complex systems but also astrophysics and the synthesis of super-heavy elements. The influence of nuclear structure on this hindrance behavior was first studied in a detailed comparison [10,13,14] for the colliding systems: ^{58}Ni + ^{58}Ni [11], ^{58}Ni + ^{60}Ni [12], ^{58}Ni + ^{64}Ni [13], and ^{64}Ni + ^{64}Ni [10], where the systems are arranged in order of decreasing stiffness. For ^{64}Ni + ^{64}Ni, an open-shell colliding system, the measured location in energy of the S-factor maximum is about 9% lower than the value expected from Eq. (2) [10], while the other systems are more in line with the systematics.

The aim of the present paper is to further investigate the hindrance phenomenon by measuring fusion evaporation for the open-shell system ^{64}Ni + ^{100}Mo. Compared to ^{64}Ni, ^{100}Mo is a transitional nucleus with two protons outside the closed proton shell. Two earlier measurements of fusion excitation functions for ^{64}Ni + ^{100}Mo can be found in the literature [15,16]. The minimum cross section measured in these two experiments is about 0.4 mb. Since the hindrance behavior is expected [from Eq. (2)] to occur at much lower energies, the main aim of the present measurement was an extension of the excitation function into the nanobarn region in order to localize and quantify this hindrance.

II. EXPERIMENTAL PROCEDURE AND RESULTS

The experiment was performed with ^{64}Ni beams in the energy range of 196–262 MeV from the superconducting linear accelerator ATLAS at Argonne National Laboratory. The maximum beam current used was ∼60 p nA. The high melting point of the target material, metallic molybdenum evaporated on a 40 μg/cm^2 carbon foil, prevented damage to the target by the relatively high beam current. The target thickness was constant during the experiment, as monitored with Si detectors. Thin targets with thicknesses of 8 or 18 μg/cm^2 were used

*Deceased.

to reduce the correction for target thickness in the energy regime of steep falloff of the excitation function. The isotopic abundance of ^{100}Mo was 97.42%, with the remainder coming from ^{98}Mo (0.96%), ^{97}Mo (0.28%), ^{96}Mo (0.34%), ^{95}Mo (0.29%), ^{94}Mo (0.18%), and ^{92}Mo (0.53%). The selection of the beam and target combination excluded the possibility of background from fusion reactions coming from beam or target contaminants [8,9]. Two surface-barrier Si detectors, located at $\pm 43^{\circ}$ with respect to the beam direction, served as monitors. The absolute cross sections for fusion evaporation were determined by using elastic scattering measured with the monitors.

The evaporation residues were identified and measured with the fragment mass analyzer (FMA) [17], which has been upgraded with the installation of a split anode in the first electric dipole [18]. The background, originating mostly from scattered beam, was greatly suppressed after this upgrade. To push the cross-section measurements to the lowest level, a new focal-plane detector with the configuration PGAC-TIC-PGAC-TIC-PGAC-IC, was used in the experiment. Here, the symbols PGAC stand for x-y position sensitive parallel grid avalanche counters, TIC for transmission ionization chambers, and IC for a large volume multianode ionization chamber. The first PGAC was mounted at the horizontal (x direction) focal plane of the FMA.

The y-focus condition occurs about 70 cm downstream of the focal plane, which is nearly at the middle of the last ionization chamber. The three sets of position signals x_1, y_1, x_2, y_2, x_3, and y_3 were measured with the three PGACs. The flight times t_2 and t_3 obtained from $\mathrm{PGAC_1}$-$\mathrm{PGAC_2}$ and $\mathrm{PGAC_1}$-$\mathrm{PGAC_3}$ were also recorded. Seven ΔE signals were measured with the ionization chambers (the first four ΔE_1–ΔE_4 in the two TICs and the last three ΔE_5–ΔE_7 in the final IC). Another time-of-flight signal t_{rf} measured the time difference between the rf system of the accelerator and the first PGAC. Three additional ΔE signals from the PGACs were also recorded. The three PGACs and two TICs operated at a fixed pressure of 3 torr of isobutane. The last ionization chamber had an adjustable pressure of 22–30 torr of isobutane. There was one 0.13 mg/cm^2 Mylar pressure foil in front of the first PGAC, and another one with a thickness of 0.22 mg/cm^2 located between the third PGAC and the last IC. This setup allowed for full tracking of each particle detected in the system and provided very good separation between evaporation residues and background events. A more detailed description of the new detector system will be published elsewhere [19].

For most settings of the FMA, two charge states of the residues were collected simultaneously. For the energies $E_{\mathrm{lab}} = 260.5$, 245.8, 209.1, 207.1, and 202.2 MeV, full charge state distributions were measured; whereas for most other energies, two FMA settings, i.e., four charge states, were recorded. At the four lowest energies, only two charge states were measured. From the full charge state distributions, charge state fractions were determined for extrapolation to all other energies. The energy distributions and angular distributions of evaporation residues were calculated with the statistical code PACE [20]. Total angular distributions for fusion evaporation have been measured in Ref. [15] for ^{64}Ni + ^{100}Mo. To check

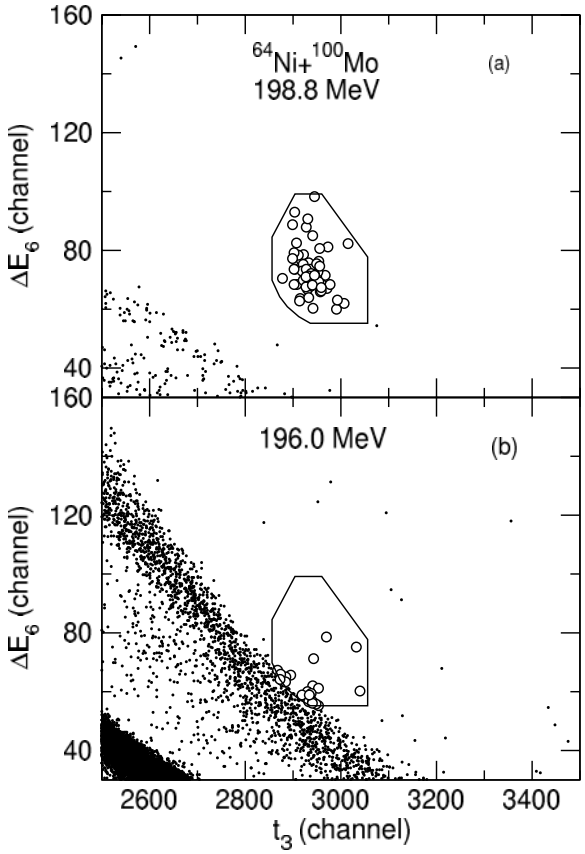

FIG. 1. Two-dimensional plots of ΔE_6 vs t_3 for the new focal-plane detector system at the FMA, obtained at two sub-barrier incident energies. (a) At 198.8 MeV, the isolated group in (open circles) originates from evaporation residues, whereas the other events are caused by background. (b) At 196.0 MeV, 23 events (open circles) fall inside the acceptance window for fusion evaporation.

the PACE code, calculations were compared with these experimental angular distributions of Ref. [15], and good agreement was found as long as the total calculated angular distributions were taken as a weighted sum of the angular distributions of the different masses from our m/q measurements and folded with multiple scattering. Whereas in Ref. [15] rather thick targets were used, the corrections from multiple scattering are small in the present experiment. The transport efficiencies of the FMA were calculated with these angular distributions, together with Monte Carlo simulations, using a modified version of the GIOS code [21]. The large momentum acceptance, $\pm 10\%$, and the large angular acceptance, $\theta_{\mathrm{lab}} < 2.3^{\circ}$, of the FMA result in a high detection efficiency for the residues.

The flight time t_3 between $\mathrm{PGAC_1}$ and $\mathrm{PGAC_3}$, together with a ΔE signal measured in a counter far behind the focal plane (e.g., ΔE_6), was found to give the best separation of the residues from background events. Two-dimensional plots of ΔE_6 vs t_3 are shown in Fig. 1, indicating the excellent separation achieved with these two quantities. Down to a cross-section level of $\sim$300 nb, the evaporation residues could be identified on the basis of these two parameters alone. The events that fall within the expected window for evaporation residues are shown as open circles in Fig. 1(a). Events shown

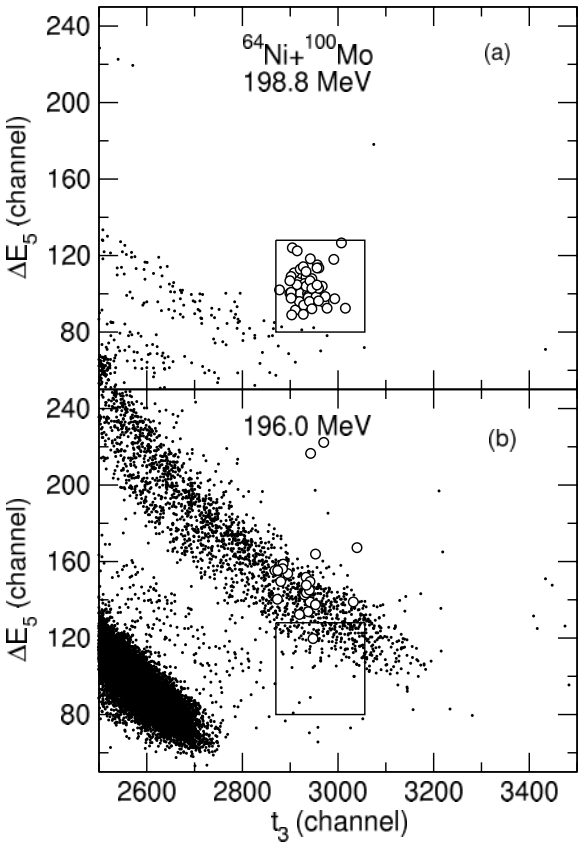

FIG. 2. Same as Fig. 1, but for ΔE_5 vs t_3. At 196.0 MeV, only one of the candidate evaporation residue events falls within the ΔE_5 range. See text for details.

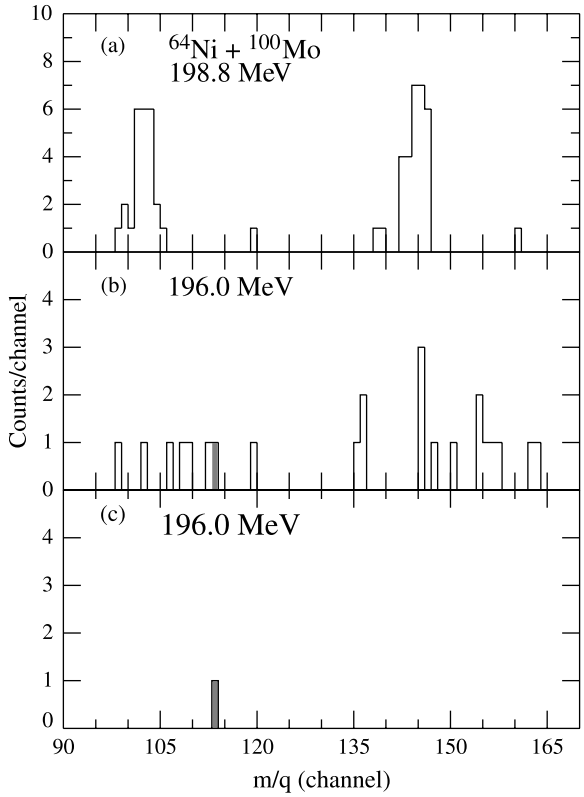

FIG. 3. Position (m/q) spectra obtained at energies of 198.8 MeV (a) and 196.0 MeV (b). These events fall inside the windows in Fig. 1(a) or 1(b), respectively. The event that also satisfies the ΔE_5 condition is marked solid grey in panels (b) and (c).

by small points originate from beam particles scattered from the beam pipe or from the area of the "beam stop" at the first split anode. The events in Fig. 1(a) correspond to a cross section of 242 nb obtained in a 12-h run. A two-dimensional plot of ΔE_5 vs t_3, corresponding to the same events, is shown in Fig. 2(a). At this energy, evaporation residues (open circles) are again well separated from background events (small points).

At the lowest energy, $E_{\text{beam}} = 196.0$ MeV, we find that 23 events fall within the expected evaporation residue window, as illustrated in Fig. 1(b). Most of these events are suspiciously close to an intense band of scattered beam particles bordering the fusion-evaporation residue window. By examining the ΔE_5 vs t_3 spectrum shown in Fig. 2(b), we see that only one of these events falls within the expected range of the ΔE_5 signal. However, this event does not have the correct m/q value, as will be demonstrated below.

An m/q spectrum containing the 23 events that fall inside the $\Delta E_6 - t_3$ window is given in Fig. 3(b). This spectrum is spread out over the whole m/q range and does not appear to be associated with the fusion-evaporation residue events seen at higher energies to be concentrated near channels 103 and 145 [see Fig. 3(a)]. The only candidate event at $E = 196.0$ MeV that satisfies the conditions for the ΔE_5, ΔE_6, and t_3 signals appears in channel 114, as seen in Fig. 3(b). By further checking all the detector signals for this event, we concluded that it is a background event, probably arising from scatterings of a beam particle at several locations through the spectrometer. Hence, only an upper limit for the measured cross section could be determined at this beam energy. These results show that a background suppression factor of about 4×10^{-17} can be achieved with the upgraded FMA and the present detector system.

The uncertainties in the reported evaporation cross sections arise mainly from corrections for the charged state distribution, FMA transport efficiency, detector efficiency, and counting statistics. The total uncertainties for the evaporation cross sections are around 10–17%, except for the measurements at the two lowest energies, where only upper limits can be given. The cross sections are listed in Table I.

The fusion-fission cross sections for ^{64}Ni + ^{100}Mo have not been measured previously. They were, however, calculated in Ref. [15] with the code CASCADE [22]. Similar calculations with the same parameters were performed for the present experiment. The total fusion cross sections are also listed in Table I, together with the fusion-fission cross sections. Rather large uncertainties were given for the fusion-fission contributions, resulting in somewhat larger errors for the total cross sections at the highest beam energies.

The experimental results for the total fusion cross sections, spanning eight orders of magnitude, are presented as a function of laboratory energy in Fig. 4 (solid circles). The incident energies have been corrected for target thickness and for the steep energy dependence; these corrections are small because

TABLE I. Measured fusion-evaporation cross sections and calculated fusion-fission cross sections (using the code CASCADE) for the ^{64}Ni + ^{100}Mo system. Large uncertainties were assigned to the calculated fusion-fission cross sections, leading to rather large errors in the total cross sections at the highest beam energies. N_q is the number of charge states for evaporation residues measured in the experiment.

$E_{c.m.}$ (MeV)	N_q	σ_{evap} (mb)	σ_{fis} (mb)	σ_{fus} (mb)
158.8	14	264 ± 35	275	539 ± 111
149.9	9	210 ± 25	80	290 ± 42
141.1	4	80.0 ± 8.8	2	82.0 ± 9.8
136.1	5	29.2 ± 3.0	0	29.0 ± 3.0
131.2	4	6.80 ± 0.71	0	6.80 ± 0.71
129.2	4	2.87 ± 0.30	0	2.87 ± 0.30
127.5	12	0.92 ± 0.10	0	0.92 ± 0.10
126.2	6	0.35 ± 0.04	0	0.35 ± 0.04
125.0	4	0.109 ± 0.012	0	0.109 ± 0.012
123.9	4	0.0253 ± 0.0029	0	0.0253 ± 0.0029
123.3	8	0.0132 ± 0.0014	0	0.0132 ± 0.0014
122.9	4	$7.4 \pm 0.87 \times 10^{-3}$	0	$7.4 \pm 0.87 \times 10^{-3}$
121.7	2	$1.10 \pm 0.16 \times 10^{-3}$	0	$1.10 \pm 0.16 \times 10^{-3}$
121.2	2	$2.42 \pm 0.41 \times 10^{-4}$	0	$2.42 \pm 0.41 \times 10^{-4}$
120.2	2	$<2.0 \times 10^{-5}$		
119.5	2	$<4.6 \times 10^{-6}$		

rather thin targets were used. For the lowest two energies, no evaporation residue was observed. The results are shown as upper limits corresponding to one count in each case. The two earlier measurements [15,16] are also shown in Fig. 4. The three measurements are generally in good agreement within the quoted uncertainties, except for the lowest energy point of Ref. [16].

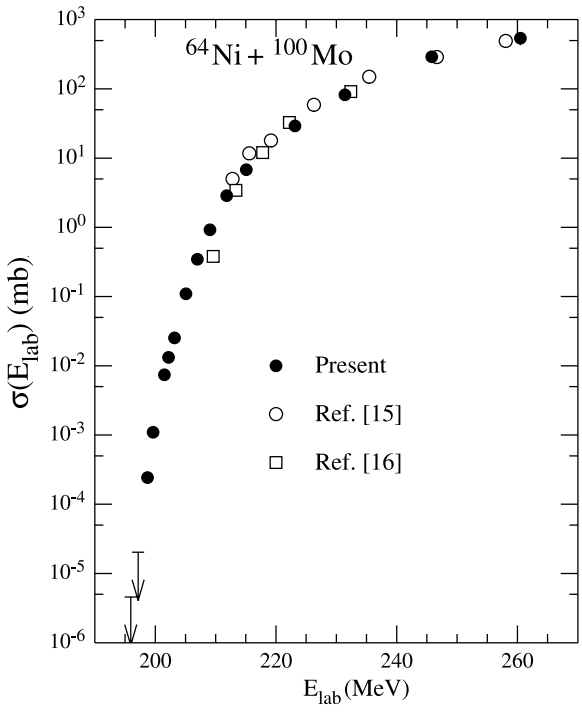

FIG. 4. Fusion excitation function for the system ^{64}Ni + ^{100}Mo (solid circles). Statistical errors are smaller than the symbol size. For the two lowest energies, no residue events have been observed. The upper limits correspond to one count. Included in the figure are two previous measurements from Refs. [15,16].

III. COUPLED-CHANNELS CALCULATIONS

The coupled-channels calculations of Ref. [15] reproduced the excitation function quite well down to the 0.5-mb level. However, with the same coupling parameters, the calculations could not account for the new data at lower beam energies. In fact, in the literature, not many such calculations can successfully reproduce experimental data for heavy systems. Since the nucleus ^{100}Mo is rather soft, multiphonon states and large coupling effects should be included in the calculations, and this represents a challenge. In the following, two sets of coupled-channels calculations are presented, including for two- and three-phonon states. The basic approach and the approximations made in these calculations using input from [23–26] are described in Ref. [27].

The nuclear structure input for the calculations is given in Table II. For ^{64}Ni it is identical to the one used in Ref. [10] to analyze the ^{64}Ni + ^{64}Ni fusion-evaporation excitation function. The nuclear quadrupole coupling, β_λ^N was set $\sim$10% higher than the value for Coulomb coupling β_λ^C (for reasons discussed in Ref. [24]). For simplicity, it was assumed that the quadrupole mode corresponds to a perfect vibrator. The structure input for ^{100}Mo is also given in Table II, whereas the experimental data used to calculate the relevant quantities for the two-phonon 2^+ excitations are listed in Table III. The nuclear β values were also set $\sim$10% higher than the Coulomb β values.

The two-phonon (2ph) calculations include the 2^+ and 3^- one-phonon states in both nuclei, the two-phonon states listed in Table II, as well as the mutual excitations of the one-phonon states. The two-phonon octupole excitation of ^{100}Mo was

TABLE II. Structure input of low-lying states in ^{64}Ni and ^{100}Mo. For ^{64}Ni, the $B(E\lambda)$ values for the quadrupole transitions are from [23,24], the octupole strength is from Ref. [25]. The ^{100}Mo input is from [26].

Nucleus	λ^π	E_x (MeV)	$B_{E\lambda}$ (W.u.)	β_λ^C	β_λ^N	Ref.
^{64}Ni	2^+	1.346	8.6	0.165	0.185	[23,24]
	2ph(2^+)	2.692	17.2	0.165	0.185	a
	3^-	3.560	12	0.193	0.200	[25]
^{100}Mo	2^+	0.536	37	0.231	0.254	[26]
	2ph(2^+)	1.002	68	0.222	0.244	b
	3ph(2^+)	1.671	90	0.206	0.215	c
	3^-	1.908	32	0.210	0.230	[26]
	2ph(3^-)	3.816	64	0.210	0.230	a

[a]Calculated assuming vibrational character.
[b]From Table III.
[c]Calculated from experimental data.

included and treated as a perfect vibrational state. Excitations above 5.5 MeV, e.g., the two-phonon 3^- state in ^{64}Ni, were not included in the coupling scheme, resulting in a total of fourteen coupled channels in the two-phonon calculation.

The three-phonon (3ph) calculations additionally included all mutual excitations of the states considered in the 2ph calculations up to two mutual two-phonon states as well as the estimated three-phonon excitation of the 2^+state in ^{100}Mo shown in Table II. However, states above 5.5 MeV were excluded, resulting in a total of 31 channels.

The ion-ion potential was parametrized as a Woods-Saxon well with a depth of $V_0 = -82.9$ MeV, diffuseness $a = 0.686$ fm, and nuclear radius $R_N = 10.19$ fm $+ \Delta R$. When the value of $\Delta R = 0.06$ fm was used in the two-phonon calculations, the result was similar to the calculations in Ref. [15] and agreed quite well with the data for the excitation function above the 1-mb level. This two-phonon calculation is shown in Fig. 5 as the dotted curve, and it is evident that it does not reproduce the data well at low energies. We also tried the recipe for using a larger diffuseness (up to $a_i = 5$ fm) inside the Coulomb barrier, which was described in Ref. [9], but this did not significantly improve the fit to the data.

A value of $\Delta R = 0.21$ fm was needed to reproduce the present data in the cross-section region of 1 to 100 μb. The potential with this ΔR value produces a Coulomb barrier

TABLE III. Experimental energies and reduced transition probabilities to the one-phonon 2^+ excitation of the two-phonon $I^\pi = 0^+$, 2^+ and 4^+ excitations in ^{100}Mo [26]. The excitation energy E_I and quadrupole transition strength of the effective 2ph(2^+) excitation are calculated according to Ref. [27].

I^π	E_I (MeV)	$B_{E2}(I \to 2)$ (W.u.)
0_2^+	0.695	92
2_2^+	1.064	51
4_1^+	1.136	69
2ph(2^{+})	1.002	68

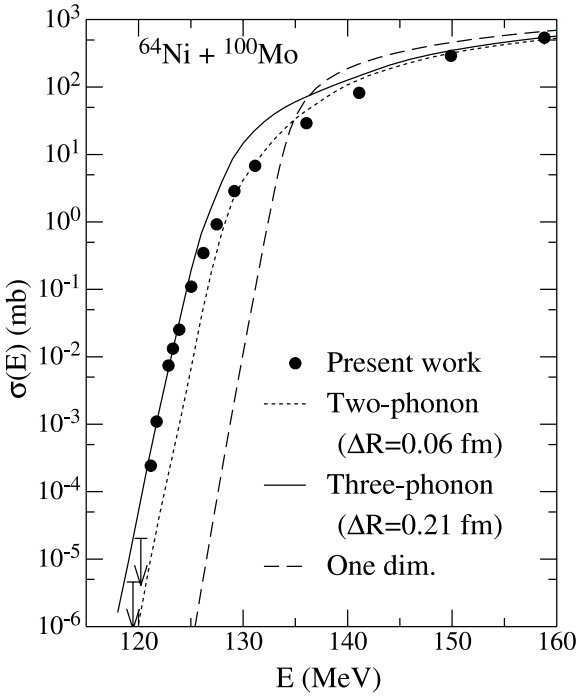

FIG. 5. Fusion excitation function for ^{64}Ni + ^{100}Mo compared with several calculations described in the text.

of 134 MeV and a pocket inside the Coulomb barrier at 112.9 MeV, which is about 20 MeV higher than the ground state energy of the compound nucleus at 92.3 MeV. The value of $\Delta R = 0.21$ fm was also adopted in the 3ph calculations. The result shown as the solid curve in Fig. 5 provides a better fit to the data in the 1 to 100 μb cross-section range. The 2ph calculation with $\Delta R = 0.21$ fm is not shown because it essentially coincides with the result for the 3ph calculation (solid curve). Both calculations reproduce the experimental data in the highest energy region and in the 1 to 100 μb range, but the cross sections in the region around $E = 130$ MeV are overpredicted. These calculations also overpredict the cross sections at the lowest energies, which is the main topic of the present study.

The long-dashed curve in Fig. 5 shows as a reference the results obtained in a one-dimensional calculation, i.e., without any couplings (with $\Delta R = 0.21$ fm). The coupled-channels calculations exhibit essentially the same energy dependence (slope) as the one-dimensional calculation when the cross sections are small (<10 μb). The coupled-channels calculations are just shifted to lower energies relative to the one-dimensional calculation. In the present case, the shift is about 7 MeV (for the same $\Delta R = 0.21$ fm). This is a general feature of coupled-channels calculations; and it is, therefore, very unlikely that any minor adjustment in the coupled-channels calculations would reproduce the steep falloff that the data exhibit at extreme sub-barrier energies. Thus, it appears that the fusion hindrance behavior, which now has been observed for many systems, is also present in the new data for ^{64}Ni + ^{100}Mo. This will be shown more convincingly in the next section, where other representations of the fusion cross section are discussed.

From the experimental data and calculations alike, one can infer a rather broad, about 18-MeV wide, barrier distribution (not shown here). An elaborate coupling scheme is therefore needed in the coupled-channels calculations. At energies above the barrier, the one-dimensional calculations result in higher cross sections than obtained by the coupled-channels calculations. This behavior is caused by the long-range Coulomb-excitation/polarization of the low-lying quadrupole states, as pointed out in Ref. [15]. As expected, the suppression of the coupled-channels fusion cross sections is rather strong in this region for the "soft" ^{100}Mo nucleus.

IV. LOGARITHMIC DERIVATIVES AND *S* FACTORS

The logarithmic derivative, $L = d\ln(\sigma E)/dE$, originally introduced in Ref. [8], is shown in Fig. 6(a) for the ^{64}Ni + ^{100}Mo system. The solid circles were obtained directly from two successive data points, whereas the stars were derived from least-squares fits to three neighboring data points. The lower limit of the logarithmic derivative was derived from the upper limit on the cross section at $E_{\text{c.m.}} = 120.2$ MeV and the data point at $E_{\text{c.m.}} = 121.2$ MeV (see Table I). The present data are compared to those of Refs. [15,16],

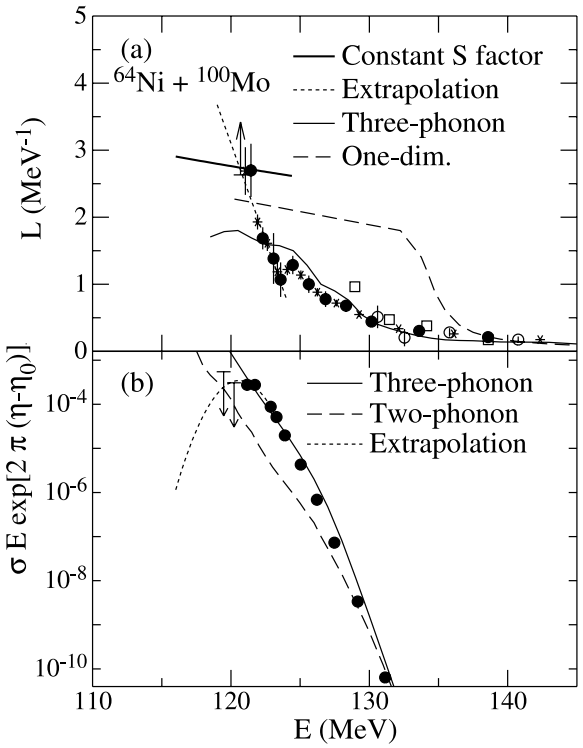

FIG. 6. (a) Logarithmic derivative representation of the ^{64}Ni + ^{100}Mo fusion excitation function. The circles were obtained from two successive data points, and stars were derived from least-squares fits to three neighboring data points. Included are the data from Ref. [15] (open circles) and Ref. [16] (open squares). (b) *S* factor representation of the same data. Calculations are shown by curves in both panels. The extrapolation curve (dotted) shown in (b) was obtained from a straight-line extrapolation of the logarithmic derivative representation in (a). A value of $\eta_0 = 105.74$ was used.

which are represented by open circles and open squares in Fig. 6(a), respectively. Only two-point derivatives are shown for these data. The three-phonon coupled-channels and the one-dimensional barrier penetration calculations are shown as solid and long-dashed curves, respectively, while the thick solid, nearly horizontal line corresponds to a constant *S* factor expression derived in Ref. [9]. The present experimental results just reach the constant *S*-factor line, implying that the experimental data have reached a maximum value for the *S* factor. The energy E_s representing the intersection between the experimental logarithmic derivatives and the constant *S*-factor line corresponds to a value of $E_s = 120.6$ MeV. The dotted line in Fig. 6(a) is an extrapolation obtained under the assumption that the logarithmic derivative is a straight line near the crossing point. This method was first introduced in Ref. [10] to obtain the extrapolated values of E_s for the systems ^{58}Ni + ^{60}Ni and ^{58}Ni + ^{64}Ni. The calculated logarithmic derivatives are seen to saturate around $L = 1.5-2$ MeV^{-1} (or start to oscillate) below $E_{\text{c.m.}} = 124$ MeV, whereas the corresponding experimental values continue to grow with decreasing energies. This saturation behavior has already been noted in Refs. [8–10].

The *S*-factor representation for the ^{64}Ni + ^{100}Mo system is presented in Fig. 6(b). As the experimental logarithmic derivatives just reach the constant *S*-factor curve, the *S*-factor maximum is not fully developed. Additional measurements would be required to clearly delineate the maximum in the *S* factor. The dotted curve corresponds to the straight-line extrapolation of the logarithmic derivative in Fig. 6(a). The two- and three-phonon calculations are shown in Fig. 6(b) as long-dashed and solid curves, respectively. It is evident that coupled-channels calculations overpredict the fusion cross section at extreme sub-barrier energies.

V. COMPARISON TO OTHER Ni-INDUCED FUSION SYSTEMS

The experimental fusion data involving Ni projectiles and compound nuclei in the $A = 100-200$ region are summarized in Table IV. For four systems, namely the ^{58}Ni + ^{58}Ni, ^{64}Ni + ^{64}Ni, ^{60}Ni + ^{89}Y, and the present ^{64}Ni + ^{100}Mo reactions, the cross sections have been measured to sufficiently low energies to determine the energy E_s of the maximum of the *S*-factor representation. In addition, we previously obtained the E_s values for the ^{58}Ni + ^{60}Ni and ^{58}Ni + ^{64}Ni systems [10] by extrapolation of the logarithmic derivative as explained below. Two additional systems, namely, ^{58}Ni + ^{74}Ge and ^{64}Ni + ^{74}Ge from Ref. [13], have been measured down to levels close to where the *S*-factor maximum occurs. The logarithmic derivative for these systems is shown in Fig. 7. The location of the *S*-factor maximum was obtained by performing a small extrapolation (solid line) of the logarithmic derivative to where it crosses the constant *S*-factor line (dashed line). The resulting values are listed in Table IV. Because of the uncertainties inherent in these extrapolations, errors of 2% (∼2 MeV) were assigned to the extrapolated E_s data, whereas an accuracy of 1% (∼2 MeV) is obtained for the four systems where a maximum in the *S* factor was observed. Table IV also lists other

TABLE IV. Parameters for Ni-induced fusion reactions on targets around the $Z, N = 28, 40$, and 50 shells. The parameters are $Z_1 Z_2 \sqrt{\mu}$ [where $\mu = A_1 A_2/(A_1 + A_2)$ is the reduced mass number of the colliding system], the crossing point energy E_s, the lowest measured energy $E_{\min}$, the reference energy E_s^{ref} obtained from Eq. (2), the ratio E_s/E_s^{ref}, the minimum cross section measured, the fusion reaction Q value, the Coulomb barrier (calculated with the Bass model [29]), and the number of "valence nucleons" N_{ph} outside the nearest closed shells. For systems that either exhibit a clear maximum in the S factor or whose logarithmic derivatives have not yet reached the constant S-factor curve but can be extrapolated to obtain the crossing point, E_s values are listed in column 3. For systems where it is not possible to make good extrapolations, the lowest measured energy is quoted in column 4. For the Ni + Sn systems, where $^{112-124}$Sn targets have been used in the measurements, only data for the ^{124}Sn target are included in the table for brevity.

System	$Z_1 Z_2 \sqrt{\mu}$	E_s (MeV)	$E_{\min}$ (MeV)	E_s^{ref} (MeV)	$\frac{E_s}{E_s^{\text{ref}}}$	$\sigma_{\min}$ (mb)	$-Q$ (MeV)	V_c (MeV)	N_{ph}	Ref.
^{58}Ni + ^{58}Ni	4222	94.0 ± 0.9		93.0	1.01 ± 0.01	0.049	66.12	102.0	2 + 2	[11]
^{58}Ni + ^{60}Ni	4258	92 ± 2		93.5	0.98 ± 0.02	0.040	62.69	101.3	2 + 4	[12]
^{58}Ni + ^{64}Ni	4325	89 ± 2		94.5	0.94 ± 0.02	0.077	53.04	100.0	2 + 4	[13]
^{64}Ni + ^{64}Ni	4435	87.7 ± 0.9		96.1	0.91 ± 0.01	$<5.3 \times 10^{-6}$	48.78	98.1	4 + 4	[10,13,14]
^{60}Ni + ^{89}Y	6537	122.9 ± 1.2		124.5	0.99 ± 0.01	$<9.5 \times 10^{-5}$	90.50	136.5	4 + 1	[8]
^{58}Ni + ^{92}Mo	7014		132.9	130.5		0.17	108.0	148.6	2 + 2	[15]
^{64}Ni + ^{92}Mo	7225		132.1	133.1		2.6	100.6	146.0	4 + 2	[15]
^{58}Ni + ^{100}Mo	7125		128.9	131.8		0.72	90.39	143.3	2 + 10	[15]
^{64}Ni + ^{100}Mo	7346	120.6 ± 1.2		134.5	0.90 ± 0.01	$<4.6 \times 10^{-6}$	92.29	136.5	4 + 10	present
^{58}Ni + ^{74}Ge	5109	98.5 ± 2.0		105.6	0.93 ± 0.02	0.037	62.03	113.4	2 + 6	[13]
^{64}Ni + ^{74}Ge	5249	97.5 ± 2.0		107.5	0.91 ± 0.02	0.013	58.48	111.3	4 + 6	[13]
^{58}Ni + ^{90}Zr	6652		127.3	125.9		0.35	97.24	141.1	2 + 0	[30]
^{58}Ni + ^{91}Zr	6666		126.4	126.1		0.25	94.18	140.8	2 + 1	[30]
^{58}Ni + ^{94}Zr	6708		122.7	126.6		0.35	86.94	139.8	2 + 4	[30]
^{64}Ni + ^{92}Zr	6881		119.0	128.8		7.5×10^{-4}	91.45	137.8	4 + 2	[31,32]
^{64}Ni + ^{96}Zr	6940		120.2	129.5		0.15	86.48	136.6	4 + 6	[31]
^{58}Ni + ^{124}Sn	8801		149.4	151.8		0.19	112.4	170.3	2 + 8	[33]
^{64}Ni + ^{124}Sn	9096		155.0	155.1		23.	117.5	167.3	4 + 8	[33]

fusion systems involving Ni beams for which the cross section was not measured down to a level that allows for determination of the S-factor maximum. For these systems, only the lowest measured energy is listed.

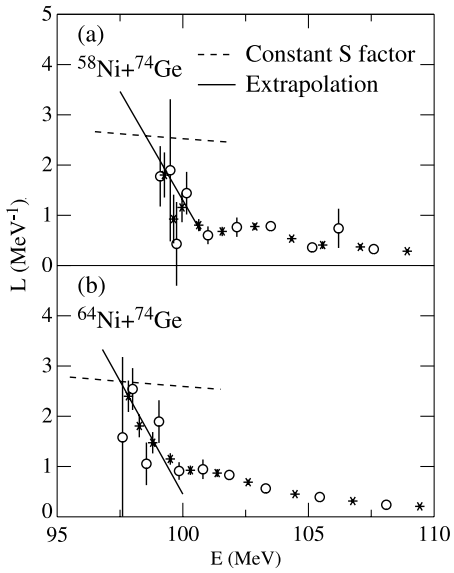

FIG. 7. Logarithmic derivative representations of the fusion data for the systems ^{58}Ni + ^{74}Ge (a) and ^{64}Ni + ^{74}Ge (b). The circles represent a simple two-point estimate of the slope, whereas the stars were obtained by a three-point least-squares fit to the data. The data are from Ref. [13].

The values of E_s are plotted as a function of the parameter $Z_1 Z_2 \sqrt{A_1 A_2/(A_1 + A_2)}$ in Fig. 8, and compared to the empirical formula (solid curve), Eq. (2), obtained from a fit to all available fusion data involving stiff nuclei. Obviously, only two systems, ^{58}Ni + ^{58}Ni and ^{60}Ni + ^{89}Y, follow the systematics; all other systems fall below the curve. We previously pointed out [10] that a rather compelling correlation exists between the stiffness of the interacting nuclei and the location of the S-factor maximum E_s relative to the empirical trend for the Ni + Ni systems. The addition to the systematics of the data points for ^{64}Ni + ^{100}Mo and for the two Ni + Ge systems, which all involve soft nuclei, appears to corroborate this observation. Thus, for the ^{64}Ni + ^{100}Mo system, the value of E_s^{ref} predicted from Eq. (2) is $E_s^{\text{ref}} = 134.5$ MeV, whereas the measured value of $E_s = 120.6$ MeV is only 90% of this value. The reason for this reduction is presumably that ^{64}Ni + ^{100}Mo should be viewed as an open-shell colliding system so that strong coupling effects broaden the effective barrier distribution and push the energy where the hindrance behavior occurs down to even lower energies.

The deviation of the measured or extrapolated values of E_s from the expected E_s^{ref} value, seen in Fig. 8, thus appears to depend on the softness of the fusing nuclei. A quantitative relation between the softness and the deviation from E_s^{ref} is not yet known. As a first attempt, we associate the stiffness of a nucleus to its proximity to closed proton or neutron shells

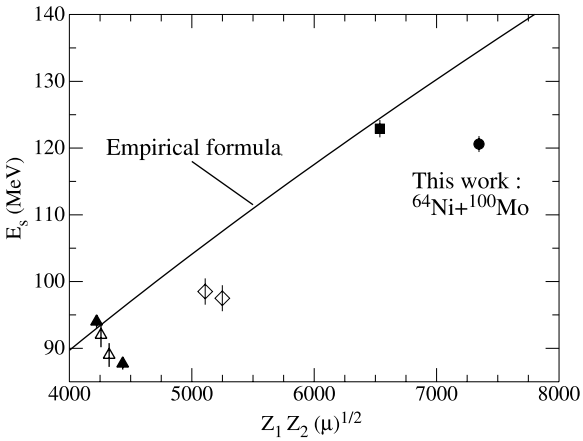

FIG. 8. Plot of E_s vs $Z_1 Z_2 \sqrt{\mu}$ for Ni bombarding different targets (see Table IV). Solid symbols correspond to systems for which the S-factor maximum is well determined: ^{58}Ni + ^{58}Ni, ^{64}Ni + ^{64}Ni, ^{60}Ni + ^{89}Y, and ^{64}Ni + ^{100}Mo. Open symbols are associated with the extrapolations for the systems ^{58}Ni + ^{60}Ni, ^{58}Ni + ^{64}Ni, ^{58}Ni + ^{74}Ge, and ^{64}Ni + ^{74}Ge. The triangles represent Ni + Ni, diamonds Ni + Ge, a square ^{60}Ni + ^{89}Y, and a circle ^{64}Ni + ^{100}Mo.

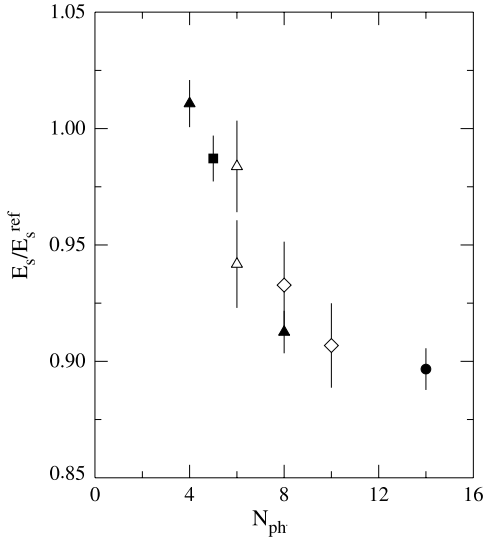

FIG. 9. Plot of $E_s/E_s^{\rm ref}$ vs $N_{\rm ph}$, where $N_{\rm ph}$ is the total number of "valence nucleons" outside closed shells in the entrance channel. Symbols are defined in Fig. 8.

and define the number of "valence nucleons" $N_{\rm ph}$ as the sum of particles and holes outside the nearest closed shells. Here, ^{64}Ni is considered to have four holes in the $N = 40$ neutron shell rather than eight particles outside $N = 28$. The values of $N_{\rm ph}$ are listed in Table IV; and in Fig. 9, the ratio $E_s/E_s^{\rm ref}$ is plotted as a function of this parameter. There is a general trend of decreasing values of $E_s/E_s^{\rm ref}$ with increasing values of $N_{\rm ph}$. We observe that for the other systems in Table IV, the data for $E_{\rm min}$ (upper limits) are not in contradiction with Figs. 8 and 9. It should be noted that all of the systems shown in Figs. 8 and 9 and Table IV have rather large negative fusion Q values. One may also compare the E_s values to the height of the Coulomb barrier (obtained from the Bass prescription), which is listed in Table IV. The ratio $E_s/E_s^{\rm ref}$ exhibits a stronger dependency on the value of $N_{\rm ph}$ than does the ratio E_s/V_c, indicating that the observed effect does not just depend on the change in the Coulomb barrier height with addition of neutrons to the interacting nuclei.

VI. DISCUSSION

The above observations are all phenomenological in nature as there is at present no satisfactory understanding of the fusion hindrance at extreme sub-barrier energies. Many authors have tried to explain this new phenomenon [28,34–38]. One suggestion is to use a large diffuseness of the ion-ion potential in the coupled-channels calculations. This recipe is sometimes used to explain high-precision fusion data [28]. It has been argued that the failure to reproduce the steep falloff is caused by the Hill-Wheeler approximation [34,35]. In Ref. [9] it was shown, however, that these limitations of the analysis are not responsible for the observed sub-barrier fusion hindrance phenomenon. Dasso and Pollarolo [36] tried to reduce the fusion cross sections by using a shallow well inside the barrier. Giraud *et al.* [37] investigated the effect of "friction." More discussions about this phenomenon can be found in Ref. [38]. All of these suggestions may improve the fit of calculations to the experimental data in some cases, but they do not provide a convincing explanation of the observed suppression in all systems. These studies are presently at the stage of raising questions and discovering weak points in the existing models. The data are most likely still insufficient to lead to the correct explanation. More precision sub-barrier fusion measurements are required to further explore which modifications in the theoretical models are relevant to a correct description of the phenomenon.

VII. SUMMARY AND CONCLUSION

The phenomenon of sub-barrier fusion hindrance was first observed in systems involving stiff nuclei, and a simple expression [9] was derived for the energy at which the hindrance of fusion between such nuclei occurs. Furthermore, a study of Ni + Ni fusion involving different Ni isotopes [10] showed that the onset of fusion hindrance deviates from these systematics depending on the "stiffness" of the interacting nuclei.

In the present work, we measured the fusion excitation function for the system ^{64}Ni + ^{100}Mo down to a cross-section level of ∼5 nb, i.e., about 12% below the Bass barrier. We observed that the fusion process is hindered at the lowest energies relative to expectations based on coupled-channels calculations. The present study of the ^{64}Ni + ^{100}Mo system shows that the fusion hindrance for this system, as well as two other soft systems, deviates strongly from the systematics, and it thus corroborates the earlier observation in Ni + Ni systems. It is furthermore shown that this deviation depends

monotonically on a parameter N_{ph}, which is the sum of nucleons (holes) outside of the closed shells of the fusing nuclei, suggesting that this parameter is a good measure of the stiffness of the interacting nuclei.

In conclusion, an interesting nuclear-structure dependence of the fusion hindrance has been observed. The origin of this effect is still unknown. It occurs at relatively high excitation energies (for systems in Figs. 8 and 9, $E_{ex} \sim 30$–40 MeV), where the natural width of compound levels is larger than their spacing. A lack of available final states thus appears to be ruled out as an explanation.

ACKNOWLEDGMENT

This work was supported by the U.S. Department of Energy, Office of Nuclear Physics, under Contract Nos. W-31-109-ENG-38 and DE-FG-06-90ER-41132.

[1] M. Beckerman, Phys. Rep. **129**, 145 (1985).
[2] M. Beckerman, Rep. Prog. Phys. **51**, 1047 (1988).
[3] R. Vandenbosch, Annu. Rev. Nucl. Part. Sci. **42**, 447 (1992).
[4] A. B. Balantekin and N. Takigawa, Rev. Mod. Phys. **70**, 77 (1998).
[5] M. Dasgupta, D. J. Hinde, N. Rowley, and A. M. Stefanini, Annu. Rev. Nucl. Part. Sci. **48**, 401 (1998).
[6] K. Hagino and N. Takigawa, Phys. Rev. C **55**, 276 (1997).
[7] N. Rowley, G. R. Satchler, and P. H. Stelson, Phys. Lett. **B254**, 25 (1991).
[8] C. L. Jiang *et al*., Phys. Rev. Lett. **89**, 052701 (2002).
[9] C. L. Jiang, H. Esbensen, B. B. Back, R. V. F. Janssens, and K. E. Rehm, Phys. Rev. C. **69**, 014604 (2004).
[10] C. L. Jiang *et al*., Phys. Rev. Lett. **93**, 012701 (2004).
[11] M. Beckerman, J. Ball, H. Enge, M. Salomaa, A. Sperduto, S. Gazes, A. DiRienzo, and J. D. Molitois, Phys. Rev. C **23**, 1581 (1982).
[12] A. M. Stefanini *et al*., Phys. Rev. Lett. **74**, 864 (1995).
[13] M. Beckerman *et al*., Phys. Rev. C **25**, 837 (1982).
[14] D. Ackermann *et al*., Nucl. Phys. **A609**, 91 (1996).
[15] K. E. Rehm, H. Esbensen, J. Gehring, B. Glagola, D. Henderson, W. Kutschera, M. Paul, F. Soramel, and A. H. Wuosmaa, Phys. Lett. **B317**, 31 (1993).
[16] M. L. Halbert, J. R. Beene, D. C. Hensley, K. Honkanen, T. M. Semkow, V. Abenante, D. G. Sarantites, and Z. Li, Phys. Rev. C. **40**, 2558 (1989).
[17] C. N. Davids and J. D. Larson, Nucl. Instrum. Methods Phys. Res. B **40/41**, 1224 (1989); C. N. Davids, B. B. Back, K. Bindra, D. J. Henderson, W. Kutschera, T. Lauritsen, Y. Nagame, P. Sugathan, A. V. Ramayya, and W. B. Walters, *ibid*. **70**, 358 (1992).
[18] C. N. Davids, ANL Phys. Div. Annual Rep. ANL-03-23, 2003, p. 104 (unpublished).
[19] C. L. Jiang *et al*., in preparation.
[20] A. Gavron, Phys. Rev. C **21**, 230 (1980).
[21] C. L. Jiang and C. N. Davids, ANL Phys. Div. Annual Rep. ANL-95/14, 1995, p. 74 (unpublished).
[22] F. Pühlhofer, Nucl. Phys. **A280**, 267 (1977).
[23] J. Charbonneau, N. V. De Castro Faria, J. L'Ecuyer, and D. Vitoux, Bull. Am. Phys. Soc. **16**, 625 (1971).
[24] F. Videbaek, P. R. Christensen, O. Hansen, and K. Ulbaek, Nucl. Phys. **A256**, 301 (1976).
[25] M. R. Braunstein, J. J. Kraushaar, R. P. Michel, J. H. Mitchell, R. J. Peterson, H. P. Blok, and H. de Vries, Phys. Rev. C **37**, 1870 (1988).
[26] B. Singh, Nucl. Data Sheets **81**, 1 (1997).
[27] H. Esbensen, Phys. Rev. C **68**, 034604 (2003).
[28] K. Hagino, N. Rowley, and M. Dasgupta, Phys. Rev. C **67**, 054603 (2003).
[29] R. Bass, Nucl. Phys. **A231**, 45 (1974).
[30] F. Scarlassara, S. Beghini, F. Soramel, S. Signorini, L. Corradi, G. Montagnoli, D. R. Napoli, A. M. Stefanini, and Z. C. Li, Z. Phys. A **338**, 171 (1991).
[31] A. M. Stefanini, L. Corradi, H. Moreno, L. Müller, D. R. Napoli, P. Spolaore, and E. Adamides, Phys. Lett. **B252**, 43 (1990).
[32] R. V. F. Janssens, R. Holzmann, W. Henning, T. L. Khoo, K. T. Lesko, G. S. F. Stephans, D. C. Radford, and A. M. Van Den Berg, Phys. Lett. **B181**, 16 (1991).
[33] W. S. Freeman, H. Ernst, D. F. Geesaman, W. Henning, T. J. Humanic, W. Kühn, G. Rosner, J. P. Schiffer, B. Zeidman, and F. W. Prosser, Phys. Rev. Lett. **50**, 1563 (1991).
[34] C. J. Lin, Phys. Rev. Lett. **91**, 229201 (2003).
[35] C. L. Jiang *et al*., Phys. Rev. Lett. **91**, 229202 (2003).
[36] C. H. Dasso and G. Pollarolo, Phys. Rev. C **68**, 054604 (2003).
[37] B. G. Giraud, S. Karataglidis, K. Amos, and B. A. Robson, Phys. Rev. C **69**, 064613 (2004).
[38] D. J. Hinde, in *Proceedings of the International Conference, Fusion 03: From a Tunneling Nuclear Microscope to Nuclear Processes in Matter, Nov. 12–15, 2003, Matsushima, Japan*, Prog. Theor. Phys. (Suppl.) **154**, 1 (2004); H. Esbensen, *ibid*. **154**, 11 (2004); C. L. Jiang, *ibid*. **154**, 61 (2004); C. J. Lin, *ibid*. **154**, 184 (2004); G. Pollaroro, *ibid*. **154**, 201 (2004); M. Dasgupta, *ibid*. **154**, 209 (2004); D. Brink, *ibid*. **154**, 268 (2004); A. B. Balantakin, *ibid*. **154**, 465 (2004).